Ultrasound tomography for simultaneous reconstruction of acoustic density, attenuation, and compressibility profiles

Pedram Mojabi[a] and Joe LoVetri

Department of Electrical and Computer Engineering, University of Manitoba, Winnipeg, Manitoba R3T 5V6, Canada

A fast and efficient forward scattering solver is developed for use in ultrasound tomography. The solver is formulated so as to enable the calculation of scattering from large and relatively high-contrast objects with inhomogeneous physical properties that vary simultaneously in acoustic attenuation, compressibility, and density. It is based on the method of moments in conjunction with a novel implementation of the conjugate gradient algorithm which requires the use of the adjoints of the scattering operators. The solver takes advantage of the symmetric block Toeplitz matrix with symmetric Toeplitz blocks property of the Green's function matrix to increase efficiency and only stores the first row of this matrix to reduce memory requirements. This row is then used for the matrix-vector multiplication using the fast Fourier transform technique, thus, resulting in the computational complexity of $O(n \log n)$. The marching-on-source technique is also used to provide a good initial guess which allows the conjugate gradient technique to converge faster than initializing with an arbitrary guess. This feature is important in tomographic inversion algorithms which require that the object to be imaged be interrogated via several incident fields. Forward scattering and inversion examples, based on the Conjugate Gradient Least Squares regularized Born Iterative Method, are shown, in two-dimensions, for objects varying in all three physical properties.
© 2015 Acoustical Society of America. [http://dx.doi.org/10.1121/1.4913774]

I. INTRODUCTION

Ultrasound tomography (UT) can be mathematically formulated as an inverse scattering problem.[1–6] In this inverse scattering problem, the goal is to find the shape, location, and some quantitative ultrasonic properties of the object of interest (OI). Images of the acoustic attenuation, compressibility, and density of materials can provide substantial information regarding the internal structure and composition of the OI. Quantitative reconstructions of these properties can be found using various nonlinear inversion algorithms. Such inversion algorithms iteratively minimize the discrepancy between measurements of scattered pressure and those simulated from predicted profiles. Thus, one important component of these inversion algorithms is the forward solver which calculates the corresponding simulated data due to a predicted profile. The main focus of this paper is the development of an appropriate forward solver for this purpose, which is then used in the Born Iterative Method (BIM)[2,5,7,8] to invert scattered pressure data and create images of three contrast parameters related to the acoustic attenuation, compressibility, and density of the OI.

In UT, the OI is surrounded by several transducers as shown in Fig. 1, and is located within a known background medium.[4,9,10] Each of these transducers can work either as a transmitter or receiver. When one transducer operates as a transmitter, the others work as receivers. This procedure

continues until all the transducers are utilized as transmitters. The pressure data at each transducer is collected in two different scenarios. The pressure data collected in the absence of the OI is called the incident pressure, and the pressure data collected in the presence of the OI is called the total pressure. The scattered pressure is then defined as the numerical difference between the total and incident pressure and serves as the measurement data that is inverted by the inversion algorithm to create one or more property images.

Some desirable features of the forward scattering solver used within the inversion algorithm are: (1) It should be able to handle inhomogeneous compressibility, density, and attenuation profiles, (2) it should handle large objects with respect to the wavelength of operation, and (3) it must be computationally and memory efficient. The first requirement is desirable so as to broaden the range of materials that can be imaged within the OI. For example, human tissue at ultrasound frequencies typically varies in all three of these properties. To the authors' knowledge, most of the forward solvers developed to-date for ultrasound imaging assume that the density profile of the OI is constant; this is true, e.g., in the biconjugate gradient imaging technique presented in Ref. 11, in the formulation of the inverse operator incorporated in the distorted Born iterative method (DBIM) as developed in Ref. 12, the parabolic approximation in Ref. 13, the multilevel fast multipole algorithm incorporated in the DBIM as developed in Ref. 14, as well as in the time-domain and frequency-domain eigenfunction methods described in Refs. 15 and 16. It is well known that the density profile in many biomedical applications such as breast imaging is not constant.[2,6,17,18] Using inversion algorithms that assume a constant density

[a]Author to whom correspondence should be addressed. Electronic mail: pedram.mojabi@gmail.com

FIG. 1. (Color online) UT setup in which the OI is enclosed by an array of ultrasound transmitters/receivers. The discretization scheme employed in this work is also shown.

profile can result in a large amount of modeling error, defined as the discrepancy between the numerical model used in the inversion algorithm and the actual measurement system, producing erroneous reconstructions. Although inversion algorithms have been reported wherein the forward solvers do not assume a constant density profile; e.g., the T-matrix and dual frequency DBIM approach as presented in Refs. 6 and 19, the fast multipole method as used in Ref. 20, and the time-domain forward solver used in Ref. 5, none of these simultaneously and quantitatively invert all three properties that are considered herein. The only work the authors are aware of where three acoustic parameters are simultaneously inverted is the work presented in Ref. 21 wherein speed of sound, density, and absorption are simultaneously inverted. It should be noted that treating these three profiles as independent unknowns have the potential to result in more accurate reconstruction accuracy in different application areas ranging from biomedical to non-destructive applications. On the other hand, this may result in the increase of the number of unknowns to be reconstructed. Therefore, more ultrasound scattering data points are then needed to be collected and used for the inversion.

The second desirable feature is due to the fact that for some biomedical UT applications, e.g., breast cancer imaging, the size of the OI is very large with respect to the wavelength of operation. This relates to the third important feature, computational efficiency, because it is typical for nonlinear inversion algorithms to call the forward solver many times for accurate quantitative reconstructions. For example, if we assume that the number of ultrasonic transducers in a UT system is 30, collecting scattered field data at 10 different frequencies, and that the inversion algorithm converges after 10 iterations, then the forward solver will be

called 3000 times. This simple example demonstrates the need for having a fast and efficient forward solver. To handle this computational burden, a forward solver based on the Neumann series was recently proposed in Ref. 2. This forward solver assumes that there exists a fixed linear relationship between the contrast of compressibility and contrast of density throughout the OI. Such an assumption is not valid for a broad range of materials and thereby limits the use of such imaging algorithms.

Finally, it is beneficial to utilize a forward solver that can handle OIs with large contrast. Sometimes the use of a proper background immersion medium, such as a matching fluid, can help reduce the contrast of the OI. When this is not feasible it is important that the forward solver be able to handle large contrast values. This is not true of the forward solver proposed in Ref. 2, which is based on the Neumann series.

In this paper, a Method of Moments (MoM)[22–25] forward solver, in conjunction with the Conjugate Gradient (CG) method,[26] is used to handle the scattering from inhomogeneous objects which simultaneously vary in compressibility, attenuation, and density. This forward solver can also deal with large high contrast objects.[3,4] To handle the computational burden associated with the UT problem, this solver is equipped with some accelerating and memory reduction features. It makes use of the block Toeplitz matrix properties[27,28] of the resulting Green's function matrices to significantly reduce the memory requirements. Second, it uses the Fast Fourier Transform (FFT) method to accelerate the matrix-vector multiplications in the CG method. Finally, the so-called marching-on-source technique is used to find a good initial guess for the CG method; thus, accelerating its convergence. To use the CG method with the integral equation formulation described herein, the adjoint of the integral operators for the inhomogeneous compressibility, attenuation, and density profiles are required. These adjoint operators are provided in the continuous domain, that is, before discretization using the MoM.

The structure of this paper is as follows. In Sec. II, we provide the mathematical formulation of the UT problem for objects having inhomogeneous complex-valued compressibility, which takes into account the attenuation and compressibility, as well as inhomogeneous density profiles. We then describe the MoM operators required in the formulation of the forward scattering problem in Sec. III, providing details on the adjoints of these operators required in the CG solution. The accelerating features of the MoM-CG forward solver are described in Sec. IV. In Sec. V we outline the BIM in conjunction with Conjugate Gradient Least Squares (CGLS) regularization which is then used to invert some two-dimensional (2D) data obtained synthetically. Although only 2D data is considered herein, the basic method is easily extended to three-dimensional (3D) problems. Section VI presents some numerical forward and inverse scattering results to demonstrate the effectiveness and efficiency of the forward solver and simultaneous reconstruction of all the contrast profiles. Discussion and conclusions are presented in Secs. VII and VIII.

II. PROBLEM FORMULATION

The acoustic wave equation can be written as[4,29–31]

$$\rho(\mathbf{r})\nabla \cdot [\rho^{-1}(\mathbf{r})\nabla p(\mathbf{r})] + \hat{k}^2(\mathbf{r})p(\mathbf{r}) = -S(\mathbf{r}), \tag{1}$$

where ρ is density, p is pressure, and S is an arbitrary acoustical source. The effect of attenuation can be modeled by assuming a complex valued wavenumber[20,30] as

$$\hat{k}(\mathbf{r}) \triangleq \frac{\omega}{c(\mathbf{r})} - j\alpha(\mathbf{r}), \tag{2}$$

where ω is the angular frequency, $c(\mathbf{r})$ is the speed of propagation, and $\alpha(\mathbf{r})$ is the attenuation. The minus sign in Eq. (2) is due to the fact a $e^{+j\omega t}$ time dependency is assumed. Similarly, the complex-valued background wavenumber, $\hat{k}_b(\mathbf{r})$, is defined as[4]

$$\hat{k}_b \triangleq \frac{\omega}{c_0} - j\alpha_0, \tag{3}$$

where $c_0(\mathbf{r})$ is the background speed of sound and $\alpha_0(\mathbf{r})$ is the background attenuation, both assumed to be constants. The scattered pressure for the inhomogeneous compressibility and density profiles can be found as[2–5]

$$p^{\text{scat}}(\mathbf{r}) = k_0^2 \int_D g(\mathbf{r}, \mathbf{r}')\chi_1^c(\mathbf{r}')p(\mathbf{r}')\mathrm{d}\mathbf{r}'$$
$$+ \int_D g(\mathbf{r}, \mathbf{r}')\nabla \cdot [\chi_2(\mathbf{r}')\nabla p(\mathbf{r}')]\mathrm{d}\mathbf{r}', \tag{4}$$

where p and p^{scat} are the total pressure and the scattered pressure. D is a domain containing the OI within the known background medium. Note that the contrast profiles, to be defined below, are zero outside D. The scattered pressure is defined as the numerical difference between the total pressure and the incident pressure, p^{inc}, that is, $p^{\text{scat}} \triangleq p - p^{\text{inc}}$. In these equations, k_0 is the real part of the complex background wavenumber, $g(\mathbf{r}, \mathbf{r}')$ is the Green's function for the background medium, and $\chi_1^c(\mathbf{r})$ is the contrast of complex compressibility. The complex compressibility profile takes into account the contrast of compressibility and the variation of attenuation via its real and imaginary parts, respectively. It is defined as[3,4]

$$\chi_1^c(\mathbf{r}) \triangleq \chi_1(\mathbf{r}) - j\frac{2\delta\alpha(\mathbf{r})}{k_0}, \tag{5}$$

where the superscript c denotes that this contrast is complex valued. The contrast of compressibility $\chi_1(\mathbf{r})$, which is real valued, is defined as

$$\chi_1(\mathbf{r}) \triangleq \frac{\kappa(\mathbf{r}) - \kappa_b}{\kappa_b}. \tag{6}$$

Here, $\kappa(\mathbf{r})$ is the compressibility at position $\mathbf{r}$ and κ_b is the background compressibility. $\delta\alpha(\mathbf{r})$ is defined as the difference between the attenuation at position $\mathbf{r}$ and the background attenuation $(\delta\alpha(\mathbf{r}) \triangleq \alpha(\mathbf{r}) - \alpha_b)$. The contrast of inverse density, $\chi_2(\mathbf{r})$, is defined as

$$\chi_2(\mathbf{r}) \triangleq \frac{\rho^{-1}(\mathbf{r}) - \rho_b^{-1}}{\rho_b^{-1}}, \tag{7}$$

where ρ_b^{-1} and $\rho^{-1}(\mathbf{r})$ are the background inverse density and the inverse density at position $\mathbf{r}$. It should be noted that Eq. (4) is derived based on Eq. (1) with the assumption of having small contrast values.[4] This completes a brief description of the acoustic scattering problem. The UT problem can then be formulated as finding $\chi_1^c(\mathbf{r})$ and $\chi_2(\mathbf{r})$ of an OI based on the knowledge of $p^{\text{scat}}(\mathbf{r})$ at certain measurement points outside the OI. To this end, we need to know the total pressure due to a predicted $\chi_1^c(\mathbf{r})$ and $\chi_2(\mathbf{r})$. This will be done through an appropriate forward solver, which is the focus of Sec. III.

III. FORWARD SOLVER

The MoM technique[22–25] has been widely used for different scattering problems to discretize the problem into a linear system of equations of the form $\mathcal{A}x = b$. In this section, the CG version of the MoM forward solver for solving the scattering from inhomogeneous attenuation, density, and compressibility profiles will be described. As noted above, the effect of inhomogeneous attenuation and compressibility will be embedded in the inhomogeneous complex compressibility profile. This CG version of the MoM forward solver requires the definition of the so-called domain operators as well as their adjoints. In Sec. III A, these adjoint operators are provided in the continuous domain. These are then discretized and used to solve the scattering problem numerically.

Two fundamental physical domains are introduced for the UT problem. The first one, called the imaging domain, contains the OI within the background medium and is denoted by D, as shown in Fig. 1. The data domain, which is outside the imaging domain, is denoted by S. This domain contains the transmitters and receivers as shown in Fig. 1. The goal of the forward solver is to determine the total pressure in the imaging domain given a transmitter location and predicted material profiles of the OI. It is assumed herein that the incident field is known analytically and the total field within D is then to be determined using Eq. (4). In this case, both r and r' in Eq. (4) belong to the imaging domain ($r, r' \in D$). Once this total pressure in D is found by the forward solver, the scattered pressure on S can be found using Eq. (4) with $r \in S$, and $r' \in D$.

A. MoM forward solver

The CG-MoM forward solver is described using two new operators which are defined as[4]

$$\mathcal{G}_{1d}(\cdot) \triangleq k_0^2 \int_D g(\mathbf{r}, \mathbf{r}')\chi_1^c(\mathbf{r}')(\cdot)\mathrm{d}\mathbf{r}', \quad \mathbf{r}, \mathbf{r}' \in D, \tag{8}$$

$$\mathcal{G}_{2d}(\cdot) \triangleq \int_D g(\mathbf{r}, \mathbf{r}')\nabla' \cdot [\chi_2(\mathbf{r}')\nabla'(\cdot)]\mathrm{d}\mathbf{r}', \quad \mathbf{r}, \mathbf{r}' \in D, \tag{9}$$

both of which operate on the total pressure in the imaging domain. The subscript d indicates that these operators are domain operators. The total-pressure equation can now be written as

J. Acoust. Soc. Am., Vol. 137, No. 4, April 2015

P. Mojabi and J. LoVetri: Ultrasound tomography   1815

$$p(\mathbf{r}) = p^{\text{inc}}(\mathbf{r}) + \mathcal{G}_{1d}\{p(\mathbf{r}')\} + \mathcal{G}_{2d}\{p(\mathbf{r}')\}$$
$$= p^{\text{inc}}(\mathbf{r}) + (\mathcal{G}_{1d} + \mathcal{G}_{2d})\{p(\mathbf{r}')\}. \qquad (10)$$

Defining $\mathcal{G}_d$ as the sum of $\mathcal{G}_{1d}$ and $\mathcal{G}_{2d}$ we have

$$(\mathcal{I} - \mathcal{G}_d)\{p(\mathbf{r})\} = p^{\text{inc}}(\mathbf{r}). \qquad (11)$$

As a linear system of equations in the form $\mathcal{A}x = b$, x is the unknown total pressure inside the imaging domain, b is the known incident pressure within the imaging domain, and the operator $\mathcal{A}$ is

$$\mathcal{A} = \mathcal{I} - \mathcal{G}_d = \mathcal{I} - \mathcal{G}_{1d} - \mathcal{G}_{2d}. \qquad (12)$$

We solve this linear-operator equation using the CG algorithm.[26] To use the CG algorithm, the adjoint of $\mathcal{A}$, denoted as $\mathcal{A}^a$, is required. The adjoint of operator $\mathcal{A}$ can be found by taking the adjoint of $\mathcal{G}_1$ and $\mathcal{G}_2$,

$$\mathcal{A}^a = (\mathcal{I} - \mathcal{G}_d)^a = (\mathcal{I} - \mathcal{G}_{1d} - \mathcal{G}_{2d})^a = \mathcal{I} - \mathcal{G}_{1d}^a - \mathcal{G}_{2d}^a. \qquad (13)$$

Therefore, to obtain $\mathcal{A}^a$, we need to determine $\mathcal{G}_1^a$ and $\mathcal{G}_2^a$. To find $\mathcal{G}_1^a$ we use the definition for the adjoint operator

$$\langle \mathcal{G}_{1d}\{p(\mathbf{r}')\}, \psi(\mathbf{r}) \rangle_D = \langle p(\mathbf{r}'), \mathcal{G}_{1d}^a\{\psi(\mathbf{r})\} \rangle_D, \qquad (14)$$

where $\langle \cdot, \cdot \rangle$ is the inner product and the subscript D denotes that this inner product is taken over the domain D. Here $\psi(\mathbf{r})$ is an arbitrary function over D. After some algebraic manipulation, the adjoint operators, $\mathcal{G}_{1d}^a$ and $\mathcal{G}_{2d}^a$, are found as

$$\mathcal{G}_{1d}^a\{\cdot\} = [k_0^2 \chi_1^c(\mathbf{r})]^* \int_D g^*(\mathbf{r}', \mathbf{r})(\cdot)d\mathbf{r}' \qquad (15)$$

and

$$\mathcal{G}_{2d}^a\{\cdot\} = \nabla \chi_2^*(\mathbf{r}) \cdot \nabla \int g^*(\mathbf{r}', \mathbf{r})(\cdot)d\mathbf{r}'$$
$$+ \chi_2^*(\mathbf{r})\nabla^2 \int g^*(\mathbf{r}', \mathbf{r})(\cdot)d\mathbf{r}', \qquad (16)$$

where * denotes the complex conjugate operation.[4] After discretizing $\mathcal{A}$ and $\mathcal{A}^a$, the CG algorithm can be applied to solve $\mathcal{A}x = b$, for the total pressure x in the imaging domain. It should be noted that the only assumption used to find the adjoint operators is that the contrast of the reciprocal of the density is zero on the boundary of D.[4] This assumption is true in practice because the OI is surrounded by the background medium, and the contrast value is zero anywhere on the background medium. That being said, it can be concluded that no approximations have been used in the derivation of this analytical formula. Note that in this paper the imaging domain is discretized into square cells using 2D pulse basis functions and Dirac delta weighting functions are utilized.[4,22–25]

The next task is to incorporate features in the numerical algorithm that will allow us to handle large numerical values of the contrast and also large objects as compared to the wavelength. The standard CG algorithm turns out to be too

computationally expensive for the UT problem. Thus, in Sec. IV we focus on three acceleration techniques that are used in conjunction with this CG-MoM forward solver.

IV. ACCELERATION TECHNIQUES FOR CG-MOM FORWARD SOLVER

As noted in Sec. I, the UT problem requires having a fast and efficient forward solver due to the fact that (1) the size of the imaging domain is usually large as compared to the wavelength of operation,[2,3] and (2) the forward solver is called several times within the utilized inversion algorithm. To handle this issue, three accelerating features are incorporated into the standard CG-MoM forward solver, which will now be described.

A. Marching-on-source technique

This technique was developed for the electromagnetic forward scattering problems.[32–34] Herein, we apply this method to the ultrasound forward scattering problem. The fundamental idea of the marching-on-source technique is to provide a good initial guess for the CG algorithm. The initial guess given to the CG algorithm plays a very important role in the number of iterations needed for its convergence. When there is no prior information related to the distribution of the total field for a given source, the initial guess is usually chosen to be either zero or the incident pressure. The intuitive idea behind the marching-on-source technique method can be explained as follows. First, note that in an UT setup, we have several transducers which are co-resident on a ring close to the OI. That we have several transducers close to the OI indicates that neighboring transducers "see" the object similarly. This indicates that the corresponding total pressure distributions of these neighboring transmitters will be similar. The level of similarity can then be determined based on comparing their incident pressure distributions. Therefore, having the total pressure distributions for some previous neighboring transducers to the transducer of interest, and knowing the incident pressure for these transducers, a good estimate for the total pressure of the transducer of interest can be calculated.

The marching-on-source technique is well suited for the UT problem in which the forward solution needs to be found for several transmitters usually located close to each other. For the first few transmitters, a typical initial guess, e.g., zero or incident pressure, is used to find the total pressure in the imaging domain. An improved initial guess for the next transmitter is then based on the total pressure that has been calculated for these previous transmitters. For example, assume that we are looking for a good initial guess for the forward scattering problem corresponding to the mth transmitter. This initial guess is written as a linear combination of Q previously found total pressures due to Q previous transmitters. The initial guess for the mth transmitter is denoted by x_m^0 and the total pressure corresponding to the $(m-q)$th transmitter is denoted by x_{m-q}. Thus, the initial guess for the mth transmitter is written as[4]

$$x_m^0 = \sum_{q=1}^{Q} a_q x_{m-q}, \qquad (17)$$

where a_q is the weighting coefficient for the total pressure inside the domain due to transmitter $m - q$. To find these coefficients, it should be noted that a good initial guess should be close to the exact solution. In other words, we minimize the following norm:[4]

$$\underset{x_m^0}{\arg\min}\{||\mathcal{A}x_m^0 - b||^2\} = \underset{a_q}{\arg\min}\left\{\left\|\sum_{q=1}^{Q} a_q \mathcal{A}x_{m-q} - b\right\|^2\right\}, \qquad (18)$$

where b is the incident field due to transmitter m. It should be noted that when $\mathcal{A}$ operates on x_{m-q}, it gives the incident pressure inside the domain due to transmitter $m - q$. Thus, Eq. (18) can be written as

$$\underset{a_q}{\arg\min}\left\{\left\|\sum_{q=1}^{Q} a_q p_{m-q}^{\text{inc}} - p_m^{\text{inc}}\right\|^2\right\}, \qquad (19)$$

where p_{m-q}^{inc} is the incident pressure inside the domain due to the transmitter $m - q$. This minimization can be written in the following form:

$$\underset{a_q}{\arg\min}\left\{\left\|(p_{m-1}^{\text{inc}} \quad p_{m-2}^{\text{inc}} \quad \cdots \quad p_{m-Q}^{\text{inc}})\begin{pmatrix} a_1 \\ a_2 \\ \vdots \\ a_Q \end{pmatrix} - p_m^{\text{inc}}\right\|^2\right\}, \qquad (20)$$

where $(p_{m-1}^{\text{inc}} \quad p_{m-2}^{\text{inc}} \quad \cdots \quad p_{m-Q}^{\text{inc}})$ is a $N \times Q$ matrix, and N is the number of cells in the imaging domain. The solution to this least-squares minimization is easily found as

$$\begin{pmatrix} a_1 \\ a_2 \\ \vdots \\ a_Q \end{pmatrix} = [(p_{m-1}^{\text{inc}} \quad p_{m-2}^{\text{inc}} \quad \cdots \quad p_{m-Q}^{\text{inc}})^H$$
$$\times (p_{m-1}^{\text{inc}} \quad p_{m-2}^{\text{inc}} \quad \cdots \quad p_{m-Q}^{\text{inc}})]^{-1}.$$
$$\times (p_{m-1}^{\text{inc}} \quad p_{m-2}^{\text{inc}} \quad \cdots \quad p_{m-Q}^{\text{inc}})^H p_m^{\text{inc}}. \qquad (21)$$

Once these coefficients are found, the appropriate initial guess can be given to the CG algorithm. Note that the calculation of these coefficients can be pre-calculated and stored since they are only dependent on the incident pressures. Therefore, their calculation does not impose any additional computational cost to the forward solver.

B. Symmetric block Toeplitz matrix with symmetric Toeplitz blocks

The other method used in this forward solver to make it efficient in terms of memory storage is based on using the block Toeplitz matrix properties. The key to this method is

that the Green's function matrix in the domain equation is a symmetric block Toeplitz matrix with symmetric Toeplitz blocks. It will be shown that only the first row of this matrix is needed to be stored instead of storing all of the matrix elements. This method was originally used in electromagnetic problems and signal processing.[27,28]

We start by noting that the term $g(\mathbf{r}, \mathbf{r}')$ is a common term in both integrals in Eq. (4). If we assume that we have a 2D time-harmonic problem with $e^{+j\omega t}$ time dependency, the Green's function for each frequency is solely dependent on the distance between positions $\mathbf{r}$ and $\mathbf{r}'$ and can be found as[6,29] $(1/4j)H_0^{(2)}(k_0|\mathbf{r} - \mathbf{r}'|)$ where H_0^2 is the zeroth-order Hankel function of the second kind. If we assume that the number of cells in the pulse basis function is $N = n_x \times n_y$ (see Fig. 1) where n_x and n_y are the number of discretized elements along the x and y axes, respectively, then each integral results in an $N \times N$ matrix of the form shown in Fig. 2. This $N \times N$ matrix is not only a symmetric block Toeplitz matrix but also each of its blocks is a symmetric Toeplitz matrix. The size of each Toeplitz matrix in Fig. 2 is $n_y \times n_y$ and the total number of Toeplitz blocks is $n_x \times n_x$. If each Toeplitz block is considered as an element of the matrix, these elements make another Toeplitz matrix.

This specific structure allows us to store only the first row of the whole matrix instead of all the N^2 elements, thus saving significantly on storage memory. As will be seen in Sec. IV C, only this first row is used for our matrix-vector multiplications. That is, the whole matrix is never actually constructed. This is possible because the CG algorithm needs only matrix-vector product operations on appropriately chosen vectors and not the actual operators themselves. Finally, we note that this Toeplitz structure can also be applied to the 3D cases.[27]

C. FFT matrix-vector multiplication

The matrix-vector multiplications required in the CG algorithm are implemented using FFT-based multiplication. This reduces the computational complexity from order
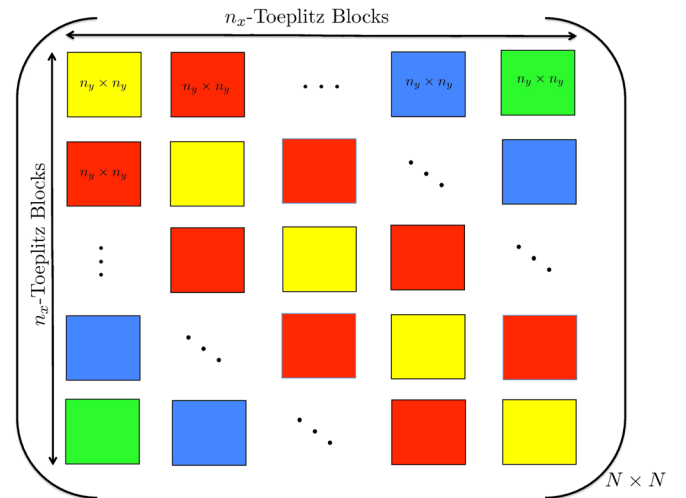

FIG. 2. (Color online) A symmetric block Toeplitz matrix. Each block is also a symmetric Toeplitz matrix of the size of $n_y \times n_y$.

FIG. 3. (Color online) Converting a symmetric Toeplitz matrix to a circulant matrix. The first block corresponds to a symmetric Toeplitz matrix. The second block is added to the first block to create a circulant matrix.

$\mathcal{O}(n^2)$ to $\mathcal{O}(n\log(n))$ as compared to performing standard matrix-vector products.

Circulant matrix-vector multiplication can be performed using the FFT multiplication.[35–38] For example, the following circulant-matrix vector multiplication can be found as

$$
\begin{pmatrix}
w_0 & w_1 & \cdots & w_{p-1} & w_p \\
w_p & w_0 & \ddots & w_{p-2} & w_{p-1} \\
\vdots & w_p & w_0 & \ddots & \vdots \\
w_2 & \ddots & w_p & \ddots & w_1 \\
w_1 & w_2 & \cdots & w_p & w_0
\end{pmatrix}
\begin{pmatrix}
k_0 \\ k_1 \\ k_2 \\ \vdots \\ k_p
\end{pmatrix}
$$
$$
= \text{IDFT}[\text{DFT}[W(1,:)] \odot \text{DFT}[K(:,1)]] , \qquad (22)
$$

where W and K are the above circulant matrix and column vector, respectively. The Hadamard product (element-wise product) is denoted by $\odot$. IDFT and DFT are the inverse discrete Fourier transform and discrete Fourier transform, respectively. $W(1,:)$ is the first row of the circulant matrix and $K(:,1)$ is the column vector that should be multiplied with a circulant matrix.

To apply this technique to the block Toeplitz matrix of Sec. IV B, each Toeplitz block is first converted to a circulant matrix. As shown in Fig. 2, the first row corresponds to the first rows of n_x Toeplitz blocks where the size of each row is n_y. Therefore, the first row of each n_x Toeplitz block is converted to the first row of a corresponding circulant matrix. This is done in a similar fashion as reported in Refs. 37 and 38, where it was shown how to convert an asymmetric Toeplitz matrix to a circulant matrix. For our symmetric Toeplitz matrix of size $n_y \times n_y$, $n_y - 2$ columns are added to this matrix as shown in Fig. 3.[4] Specifically, a matrix having the elements shown in the second box, which has a size of $n_y \times (n_y - 2)$, is added to the original matrix shown in the first box. This converts our matrix to a circulant matrix. As before, this is created implicitly via the first row only. That is, $n_y - 2$ elements are added to the first row of each Toeplitz matrix. Note that this conversion makes the size of the corresponding vector to be multiplied differently than in the original multiplication. This means that $n_y - 2$ elements should also be added to the corresponding vector that is to be multiplied. These elements are denoted by $c_1, c_2, ..., c_{n_y-2}$. To have the same results for both matrix-vector multiplications as shown in Fig. 4, (1) the value of $c_1, c_2, ..., c_{n_y-2}$ are set to zero and (2) the last $n_y - 2$ elements of resulting vector after multiplication are removed.

FIG. 4. (Color online) A circulant matrix-vector multiplication and a Toepliz matrix-vector multiplication.

P. Mojabi and J. LoVetri: Ultrasound tomography

This procedure is performed for the first row of each n_x Toeplitz matrices and column vectors that correspond to these Toeplitz matrices.

The basic idea behind the FFT matrix-vector multiplication for this matrix can now be summarized as follows. To this end, consider the matrix shown in Fig. 2 that consists of n_x block rows. Since the whole matrix is symmetric block Toeplitz, all the block rows can be simply generated merely by knowing the first block row. In addition, since the first block row consists of Toeplitz matrices, its first row can be simply used to generate the whole block row. Therefore, the very first row of the first block row can represent the entire matrix. That is why we only store this single row instead of the entire matrix. Also, as described above, this single row can be used with the FFT to operate on a vector of appropriate size so as to implicitly calculate the operation of the entire matrix on that vector. To this end, this single row needs to be divided into n_x parts, each of which belongs to one of the n_x different Toeplitz matrices of the first block row. Likewise, the vector by which the entire matrix is to be multiplied is divided into n_x parts. These n_x parts of the first row operate on the corresponding n_x parts of the vector. The results of these n_x operations will then be summed up to produce the result of the operation of the first block row on the vector. Using the result of this calculation, and re-ordering them, the results of the operation of other block rows on that vector can also be found. Therefore, the result of the operation of the entire matrix on that vector is now found.

Finally, we note that the whole idea behind this acceleration lies in the fact that the Green's function relies on $|\mathbf{r} - \mathbf{r}'|$. Since the complex conjugate of the Green's function also shares this property, the adjoint of the forward operators can also be accelerated using this technique. (Note that these adjoint operators utilize the complex conjugate of this Green's function in their kernels.)

V. INVERSION ALGORITHM

A. BIM

The BIM is used as the non-linear inversion algorithm to simultaneously reconstruct the contrast profiles. In the BIM, we start by assuming that the unknown total pressure distribution within the imaging domain is the same as the known incident pressure distribution. Using this approximation, we then solve for the contrast profiles. These predicted contrast profiles are then used to find a new total pressure distribution within the imaging domain. Using the new predicted total pressure distribution, the new predicted contrast profiles are found. This procedure continues until the convergence criterion is met. The steps of this algorithm can then be summarized as:[2,5,7,8,39]

(1) Set the unknown total pressure inside the imaging domain to be equal to the incident pressure in the first iteration (Born approximation), which is utilized in Eqs. (24) and (25).
(2) Find the contrasts of OI by solving the resulting linearized integral equation (see Secs. V B and V C).

(3) Call the forward solver to find the total pressure inside the imaging domain based on the predicted contrast profiles of the previous step (see Sec. III A). To accelerate the forward solver, we utilize the method explained in Sec. IV.
(4) Find the simulated scattered pressure at the receiver locations based on the calculated total pressure in the previous step.
(5) Calculate the discrepancy between the measured and simulated scattered pressure (data misfit).
(6) Go back to step (2) until the data misfit becomes sufficiently small.

Finally, as noted in Ref. 40, the BIM is capable of handling multiple-scattering events within the OI. The BIM achieves this via its iterative nature. Intuitively speaking, each iteration of the BIM attempts to recover one scattering event.

B. Data operator

To find the contrast profiles, a linear equation, $\mathcal{A}x = b$, for the scattered pressure at the receiver points, b, is formulated where x now contains the discretized values of the unknown contrast profiles, and $\mathcal{A}$ is now the data operator that takes these contrast profile values and calculates the scattered pressure at the receiver locations. This data operator is decomposed into two operators denoted by $\mathcal{G}_{1s}$ and $\mathcal{G}_{2s}$. The scattered pressure based on these operators can be written as[1]

$$p^{\text{scat}}(\mathbf{r}) = \mathcal{G}_{1s}\{\chi_1^c(\mathbf{r}')\} + \mathcal{G}_{2s}\{\chi_2(\mathbf{r}')\}, \tag{23}$$

where subscript s denotes that these operators output field variables on the S domain. $\mathcal{G}_{1s}$ and $\mathcal{G}_{2s}$ operate on the complex contrast of compressibility and contrast of inverse density and are defined as

$$\mathcal{G}_{1s}(\cdot) \triangleq k_0^2 \int_D g(\mathbf{r}, \mathbf{r}')(\cdot)p(\mathbf{r}')\mathrm{d}\mathbf{r}', \quad \mathbf{r}' \in D, \mathbf{r} \in S, \tag{24}$$

$$\mathcal{G}_{2s}(\cdot) \triangleq \int_D g(\mathbf{r}, \mathbf{r}')\nabla \cdot [(\cdot)\nabla p(\mathbf{r}')]\mathrm{d}\mathbf{r}', \quad \mathbf{r}' \in D, \mathbf{r} \in S. \tag{25}$$

When discretized, the data equation produces an ill-conditioned matrix equation which requires regularization to invert. We perform this regularization using the CGLS technique which will be described in Sec. V C. The CGLS algorithm requires the use of the adjoint of the data operator which operates on field values of S. These adjoints can be found as[1,2,4]

$$\mathcal{G}_{1s}^a\{\cdot\} = [k_0^2 p(\mathbf{r}')]^* \int_S g^*(\mathbf{r}, \mathbf{r}')(\cdot)\mathrm{d}\mathbf{r}, \tag{26}$$

$$\mathcal{G}_{2s}^a\{\cdot\} = -\nabla' p^*(\mathbf{r}') \cdot \nabla' \int_S g^*(\mathbf{r}, \mathbf{r}')(\cdot)\mathrm{d}\mathbf{r}. \tag{27}$$

C. CGLS regularization

The UT problem is an ill-posed problem which requires a regularization technique to obtain a physical solution. The

CGLS regularization used herein is a well-known technique which implicitly effects the truncated singular-value decomposition for solving the ill-conditioned matrix that results from discretizing the data operator.[41–43] The main reason for choosing this regularization is the computational efficiency with which it can be implemented for our UT problem. In the implementation of BIM for our problem, at each step (2) the data operator changes because the total field inside D is updated. Thus, it is not efficient to store the complicated matrix representation corresponding to these new data and adjoint operators at each step in the BIM iterations. This is easily accommodated by CGLS because it only requires matrix-vector multiplications which represent the action of the data operator on contrast values and the operation of the data-operator adjoint on discretized functions defined on S. Therefore, it does not require the full storage of the matrix representing the data operator and its adjoint (even if it could be found).

The CGLS method projects the solution into a Krylov subspace for the problem at each of its iterations.[43,44] The CGLS iteration loop must be terminated to obtain a stable solution to the poorly conditioned matrix equation. At early iterations of the BIM, where the estimation of the total field within the imaging domain is poor, the CGLS iterations are terminated early. This corresponds to approximating the contrast using low spatial frequency components. As the BIM gets closer to the solution, higher frequency components for the contrast can be determined using CGLS by allowing more iterations. This *ad hoc* technique was proposed in Ref. 42 to terminate the CGLS iterations for microwave imaging algorithms. The number of CGLS iterations, which determine the final size of the Krylov subspace being projected onto, acts as a regularization parameter in CGLS regularization. The details of this regularization technique are explained in Refs. 4, 42, and 43.

Finally, we again emphasize that the computational efficiency of the CGLS algorithm which requires only a few matrix-vector multiplications is an important advantage of this regularization technique. In addition, that the CGLS regularization method does not require the full storage of the matrix provides another important advantage for this method especially when dealing with large scale problems. On the other hand, the appropriate dimension of the Krylov subspace should be determined using *ad hoc* techniques.[42]

VI. RESULTS

A. Forward solver

In this section, the effects of the accelerating features of the CG-MoM forward solver are demonstrated. We first tabulate the computational time required for standard matrix-vector multiplication compared with the case that only the first row of the matrix is stored and FFT matrix-vector multiplication is utilized. We next show the effect of marching-on-source on the convergence of the CG algorithm, by applying the forward solver to a scattering problem which contains inhomogeneities in all three physical acoustic parameters.

Consider imaging domains of various increasing sizes with respect to the wavelength. Imaging domains for 16 different cases are tabulated in Table I, where the domain size

TABLE I. Calculation time required for the standard matrix storage and matrix-vector multiplication as compared to the time required for storage and matrix-vector multiplication as presented in this paper.

Case	n_x	n_y	Domain size	T_1 [s]	T_2 [s]	T_3 [s]	T_4 [s]
1	20	20	$2\lambda \times 2\lambda$	0.26	0.009	0.02	0.007
2	40	40	$4\lambda \times 4\lambda$	2.86	0.012	0.021	0.013
3	60	60	$6\lambda \times 6\lambda$	12.97	0.070	0.023	0.045
4	80	80	$8\lambda \times 8\lambda$	40.27	0.225	0.027	0.052
5	100	100	$10\lambda \times 10\lambda$	89.69	0.495	0.029	0.065
6	120	120	$12\lambda \times 12\lambda$	188.2	1.034	0.034	0.103
7	140	140	$14\lambda \times 14\lambda$	326.3	1.84	0.041	0.378
8	160	160	$16\lambda \times 16\lambda$	1324	23.74	0.047	0.464
9	180	180	$18\lambda \times 18\lambda$	5836	1979	0.053	0.545
10	200	200	$20\lambda \times 20\lambda$	11387	4094	0.061	0.655
11	220	220	$22\lambda \times 22\lambda$			0.069	0.817
12	300	300	$30\lambda \times 30\lambda$			0.1132	4.4582
13	400	400	$40\lambda \times 40\lambda$			0.1707	7.681
14	500	500	$50\lambda \times 50\lambda$			0.236	12.32
15	1000	1000	$100\lambda \times 100\lambda$			0.8614	97.36
16	1500	1500	$150\lambda \times 150\lambda$			1.9763	471.3

n_x: Number of discretized elements in the x axis.
n_y: Number of discretized elements in the y axis.
T_1: Time taken to make the whole matrix.
T_2: Time taken for standard matrix-vector multiplication.
T_3: Time taken to make the first row of the matrix.
T_4: Time taken to perform FFT matrix-vector multiplication by using the first row of the matrix.

varies from $2\lambda \times 2\lambda$ to $150\lambda \times 150\lambda$. The number of unknowns in the domain increases dramatically, given as $n_x \times n_y$, where we have considered a minimum discretization requirement of ten cells per wavelength. For small domains the time required to store the whole matrix (T_1) and the time required to perform standard matrix-vector multiplication (T_2) are almost comparable to the time required for storing the first row of the matrix (T_3), and the time required to perform FFT matrix-vector multiplication using only this row (T_4). However, as the size of the imaging domain increases, the values of T_1 and T_2 become significantly larger. Specifically, when the size of the imaging domain reaches $22\lambda \times 22\lambda$, the standard method, when implemented on MATLAB running on a computer with 32 GB of RAM, fails to provide the matrix-vector multiplication due to lack of memory. However, on the same computer, MATLAB took less than a second to calculate the same matrix-vector multiplication that the standard method fails to calculate. Interestingly, when the size of the imaging domain reaches $100\lambda \times 100\lambda$, the proposed method takes less than 100 s to calculate the matrix-vector multiplication. Therefore, the use of such fast and efficient forward solvers is essential to solving UT problems.

UT problems also typically have a large number of incident fields where the marching-on-source technique is able to find a good initial guess for the CG algorithm, thus leading to faster convergence. To demonstrate this feature of our forward solver, consider a 2D scattering problem consisting of four cylinders each having a diameter of 4λ. This scattering object is enclosed within a $15\lambda \times 15\lambda$ imaging domain and the frequency of operation is 250 kHz. The total number

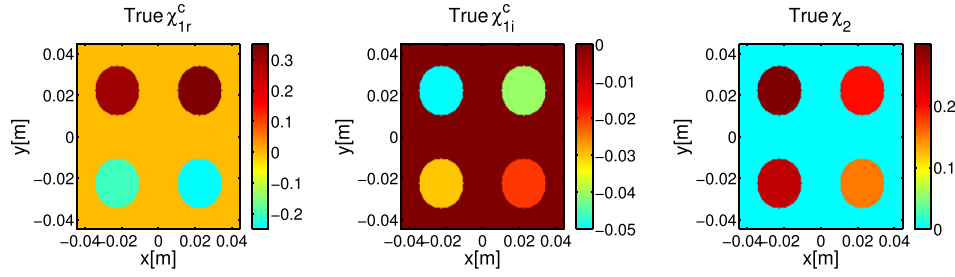P. Mojabi and J. LoVetri: Ultrasound tomography

FIG. 5. (Color online) True contrast profiles for comparison between the final calculated total pressure within the imaging domain with two different initial guesses.

of transducers used in this example is 400. (It should be noted that recent UT systems often have many more transducers. For example, in Refs. 45 and 46, 2048 transducers are used in a ring.) The UT properties (χ_1^c and χ_2) of this OI are shown in Fig. 5. In this example, the total pressure in the imaging domain for the first Q transmitters is found using our forward solver when the incident pressure is given as the initial guess to the CG algorithm. The calculation of the total pressure corresponding to the remaining transmitters is substantially accelerated by the use of the marching-on-source technique, which uses the already-calculated total pressure of the previous transmitters. Table II shows the number of CG iterations needed to converge to the solutions for the first 20 transmitters using 6 different categories of initial guesses.

TABLE II. Comparison between the number of CG iterations required for converging to the solution for some transmitters using six different initial guesses. The first one uses the incident pressure as the initial guess, and the remaining columns show results using the marching-on-source technique with varying Q to generate the initial guess.

Transmitter Index	C_1	C_2	C_3	C_4	C_5	C_6
Tx_1	178	178	178	178	178	178
Tx_2	178	178	178	178	178	178
Tx_3	179	92	179	179	179	179
Tx_4	179	96	86	179	179	179
Tx_5	181	91	90	57	181	181
Tx_6	181	93	86	71	31	181
Tx_7	181	93	88	60	52	23
Tx_8	180	91	83	73	50	44
Tx_9	180	90	84	53	57	46
Tx_{10}	180	90	83	67	65	70
Tx_{11}	180	89	84	69	64	85
Tx_{12}	180	89	81	76	76	92
Tx_{13}	180	88	80	66	80	102
Tx_{14}	180	89	78	76	89	99
Tx_{15}	180	89	79	65	94	106
Tx_{16}	180	89	78	77	93	116
Tx_{17}	179	88	77	74	98	135
Tx_{18}	177	87	76	81	97	131
Tx_{19}	176	88	76	77	97	126
Tx_{20}	175	89	77	80	100	173

Required iterations for the CG algorithm using the following initial guesses:
C_1: Incident pressure.
C_2: Marching-on-source Technique with $Q = 2$.
C_3: Marching-on-source Technique with $Q = 3$.
C_4: Marching-on-source Technique with $Q = 4$.
C_5: Marching-on-source Technique with $Q = 5$.
C_6: Marching-on-source Technique with $Q = 6$.

The first column, denoted by C_1, simply uses the incident pressure as the initial guess. In the remaining five columns of Table II, we show the required CG iterations based on using the marching-on-source technique with varying values of Q, ranging from 2 to 6. For this example, using the marching-on-source technique using the previous four transmitters, $Q = 4$, leads to an overall fewer number of CG iterations. Using more transmitters may not lead to a better initial guess if the total field due to the transmitters used in the linear approximation is not very similar. Therefore, the criteria of using $Q = 4$ will change depending on the separation between transmitters.

B. Inversion results

We now consider a total of four different 2D inversion examples based on synthetically generated data. The first two examples have imaging domains that are $8\lambda_{min} \times 8\lambda_{min}$, and contain two cylinders each. In the first, the two cylinders have the same physical properties whereas in the second the two cylinders differ. The third example has a much larger imaging domain of $15\lambda_{min} \times 15\lambda_{min}$ and contains two identical cylinders. The fourth example is a very large problem of $20\lambda_{min} \times 20\lambda_{min}$ and contains two cylinders where now the density is assumed to be the same as the background, that is, $\chi_2 = 0$. A summary of the information regarding the number of transmitters, receivers, domain size, the diameter of the OI, frequency of operations, and the contrast profiles of the OI for all these example are listed in Table III. In all examples, three percent noise, NP = 3%, is added to the synthetic data using the following formula:

$$p_{noisy}^{scat} = p_{simulated}^{scat} + |\overline{p_{simulated}^{scat}}| \times \frac{NP \times RV}{\sqrt{2}}, \quad (28)$$

where $-1 < RV < 1$ is a uniformly distributed random vector. The range of frequencies utilized for the inversions is $200 \leq f \leq 270$ kHz. The multiple-frequency data sets are utilized simultaneously to reconstruct the contrast profiles of the OI.[1,47,48] Assuming we have data from nRx receivers, nTx transmitters, and at n_f frequencies, then the total amount of information used by the inversion algorithm at each frequency is $nRx \times nTx$. Thus, inverting using all frequencies simultaneously results in n_f complex valued data-vectors of length $nRx \times nTx$ concatenated into a single vector of length $nRx \times nTx \times n_f$. For these examples the background medium is chosen to be water where the speed of the sound is

J. Acoust. Soc. Am., Vol. 137, No. 4, April 2015

P. Mojabi and J. LoVetri: Ultrasound tomography   1821

TABLE III. The information of the examples shown in the inversion results. nRx and nTx denote the number of transmitters and receivers, respectively.

Example	nTx	nRx	Size Domain	Diameter OI	Frequencies [kHz]	Cylinder 1	Cylinder 2
1	100	100	$8\lambda_{\min} \times 8\lambda_{\min}$	$2\lambda_{\min}$	$\begin{cases} f_1 = 250 \\ f_2 = 260 \\ f_3 = 270 \end{cases}$	$\begin{cases} \chi_{1r} = 0.15 \\ \chi_{1i} = -0.08 \\ \chi_2 = 0.1 \end{cases}$	$\begin{cases} \chi_{1r} = 0.15 \\ \chi_{1i} = -0.08 \\ \chi_2 = 0.1 \end{cases}$
2	100	100	$8\lambda_{\min} \times 8\lambda_{\min}$	$2\lambda_{\min}$	$\begin{cases} f_1 = 250 \\ f_2 = 260 \\ f_3 = 270 \end{cases}$	$\begin{cases} \chi_{1r} = 0.2 \\ \chi_{1i} = -0.03 \\ \chi_2 = 0.08 \end{cases}$	$\begin{cases} \chi_{1r} = 0.1 \\ \chi_{1i} = -0.06 \\ \chi_2 = 0.05 \end{cases}$
3	120	120	$15\lambda_{\min} \times 15\lambda_{\min}$	$4\lambda_{\min}$	$\begin{cases} f_1 = 200 \\ f_2 = 210 \\ f_3 = 220 \\ f_4 = 230 \\ f_5 = 240 \end{cases}$	$\begin{cases} \chi_{1r} = 0.14 \\ \chi_{1i} = -0.08 \\ \chi_2 = 0.1 \end{cases}$	$\begin{cases} \chi_{1r} = 0.14 \\ \chi_{1i} = -0.08 \\ \chi_2 = 0.1 \end{cases}$
4	200	200	$20\lambda_{\min} \times 20\lambda_{\min}$	$5\lambda_{\min}$	$\begin{cases} f_1 = 200 \\ f_2 = 210 \\ f_3 = 220 \\ f_4 = 230 \end{cases}$	$\begin{cases} \chi_{1r} = 0.07 \\ \chi_{1i} = -0.03 \\ \chi_2 = 0 \end{cases}$	$\begin{cases} \chi_{1r} = -0.07 \\ \chi_{1i} = -0.05 \\ \chi_2 = 0 \end{cases}$

set to $c_b = 1483$ [m/s]. Contrast values for these examples are chosen within ranges corresponding to the physical parameters of human tissue. These specific contrast values are within the range of values typically used to model breast tissues, as reported in Ref. 2.

The first example considers the reconstruction of two cylinders, each having a diameter of $2\lambda_{\min}$ and the contrast profiles of $\chi_1^c = 0.15 - j0.08$ and $\chi_2 = 0.1$, enclosed within an $8\lambda_{\min} \times 8\lambda_{\min}$ imaging domain, as shown in the first row of Fig. 6. Three frequencies, $f = [250, 260, 270]$ kHz, are simultaneously used for the reconstruction. Thus, at these chosen frequencies the minimum wavelength with respect to the background medium is $\lambda_{\min} \simeq 5.5$ mm. The number of transmitters and receivers utilized in this example are 100. The BIM with CGLS regularization inversion algorithm took only ten iterations to converge. The reconstruction of the contrast profiles for the tenth iteration of the BIM is shown in the second row of Fig. 6. The results of the comparison between the exact value of the contrast profiles with the reconstructed contrast profiles for the pixels on the main diagonal are shown in Fig. 7. The first and second rows of this figure correspond to the reconstruction of the contrast profiles after the first and tenth iterations of

the BIM. The number of CGLS iterations was set to 2 in the first iteration and was increased systematically, reaching a value of 200 by the tenth iteration. As can be seen in Fig. 7, the first iteration of the BIM (Born approximation) provides a reasonable qualitative reconstruction of the two cylinders but does not reconstruct the actual values of the contrasts well. By the tenth iteration the BIM achieves good accuracy in reconstructing these values.

The second example is similar to the first, but the contrasts of the two cylinders differ. The contrast profiles for the top cylinder is $\chi_1^c = 0.2 - j0.03$, $\chi_2 = 0.08$ and the contrast profiles for the bottom cylinder is $\chi_1^c = 0.1 - j0.06$, $\chi_2 = 0.05$, as shown in the top row of Fig. 8. The BIM converged at the tenth iteration and the final contrast profiles are shown in the second row of Fig. 8. The exact value of the contrast profiles as well as the reconstructed contrast profiles for the elements on the main diagonal are shown in Fig. 9. The number of CGLS iterations at the last iteration of the BIM was set to 200.

The reconstruction of two cylinders each with a diameter of $4\lambda_{\min}$ and contrast profiles of $\chi_1^c = 0.14 - j0.08$ and $\chi_2 = 0.1$ enclosed within $15\lambda_{\min} \times 15\lambda_{\min}$ imaging domain is considered next. The true profiles are shown in
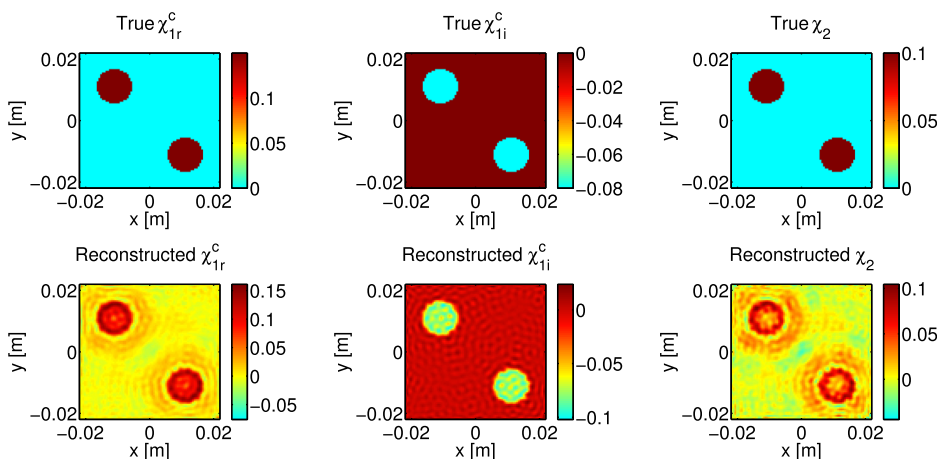

FIG. 6. (Color online) Simultaneous reconstruction of χ_1^c and χ_2 for two cylinders with the same contrast profiles enclosed within a $8\lambda_{\min} \times 8\lambda_{\min}$. The first row is the true contrast profiles. The second row corresponds to the reconstruction of contrast profiles for the tenth iteration of the BIM.

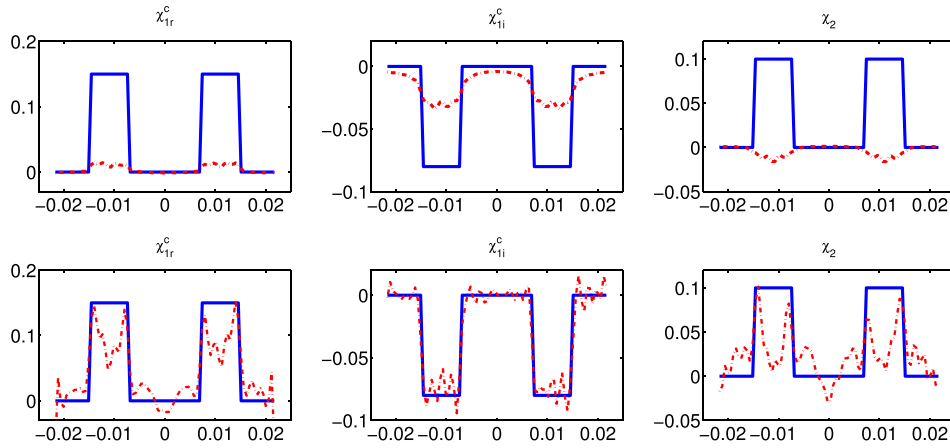P. Mojabi and J. LoVetri: Ultrasound tomography

FIG. 7. (Color online) Diagonal cut from the top left to the bottom right for the case that the OI consists of two cylinders with the same contrast profiles. The first and second rows correspond to the first and tenth iterations of the BIM. The solid line corresponds to the actual contrast profiles and the dashed line corresponds to the reconstructed contrast profiles.
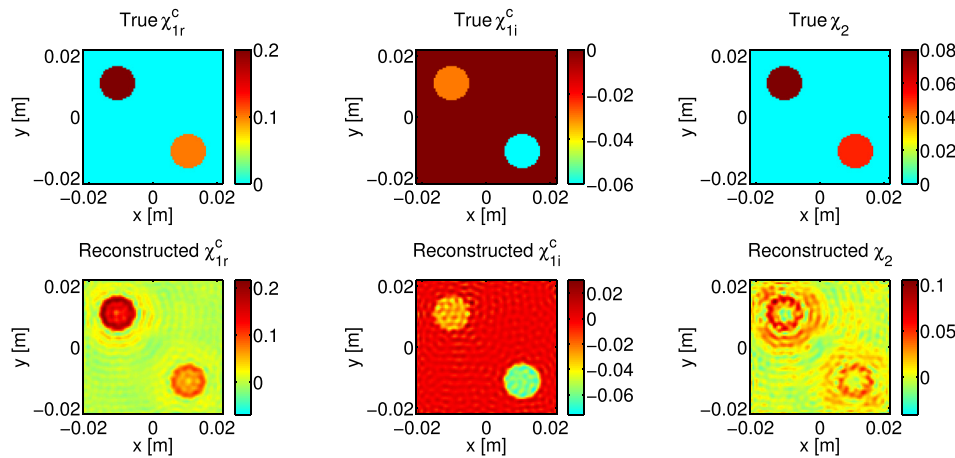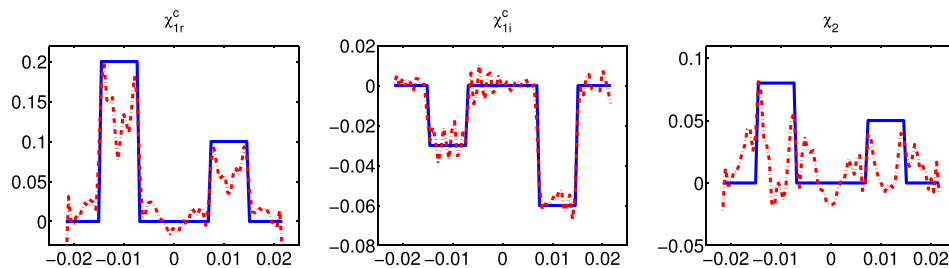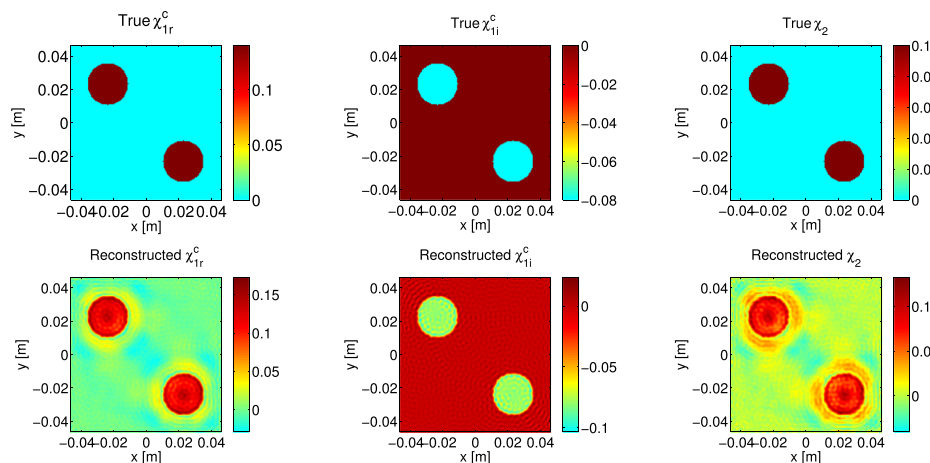

FIG. 8. (Color online) Simultaneous reconstruction of χ_1^c and χ_2 for two cylinders with the different contrast profiles enclosed within a $8\lambda_{min} \times 8\lambda_{min}$. The first row is the true contrast profiles. The second row corresponds to the reconstruction of contrast profiles for the tenth iteration of the BIM.

FIG. 9. (Color online) Diagonal cut from the top left to the bottom right for the case that the OI consists of two cylinders with different contrast profiles. It corresponds to the tenth iteration of the BIM. The solid line corresponds to the actual contrast profiles and the dashed line corresponds to the reconstructed contrast profiles.

FIG. 10. (Color online) Simultaneous reconstruction of χ_1^c and χ_2 for two cylinders with the same contrast profiles enclosed within a $15\lambda_{min} \times 15\lambda_{min}$. The first row shows the true contrast profiles. The second row corresponds to the reconstruction of contrast profiles for the eighth iteration of the BIM.
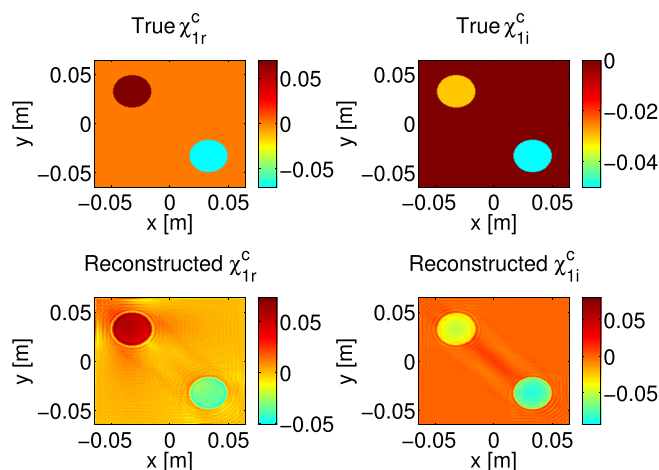
FIG. 11. (Color online) Simultaneous reconstruction of χ_1^c for two cylinders with different contrast profiles enclosed within a $20\lambda_{min} \times 20\lambda_{min}$ imaging domain. The first row shows the true contrast profiles. The density is assumed to be constant and equal to that of the background. The second row corresponds to the reconstruction of the contrast profiles for the fourth iteration of the BIM.

the first row of Fig. 10. The number of transmitters and receivers were increased to 120 for this example and now 5 frequencies, $f = [200, 210, 220, 230, 240]$ kHz, were simultaneously used for the inversion. Thus, the minimum wavelength at these chosen frequencies is $\lambda_{min} \simeq 6.18$ mm. The reconstructions of the contrast profiles for the eighth iteration of the BIM, in which the maximum number of CGLS iterations was set to 200, are shown in the second row of Fig. 10.

The final example shows the reconstruction of two cylinders each having a diameter of $5\lambda_{min}$ and contrast profiles of $\chi_1^c = 0.07 - j0.03$ and $\chi_1^c = -0.07 - j0.05$ enclosed within $20\lambda_{min} \times 20\lambda_{min}$ imaging domain. The density is assumed to be the same as the background, giving $\chi_2 = 0$. The true profiles are shown in the first row of Fig. 11. The number of transmitters and receivers for this example was set to 200. Four frequencies, $f = [200, 210, 220, 230]$ kHz, were used for the inversion. The reconstructions of the contrast profiles for the fourth iteration of the BIM in which the number of CGLS iterations was set to 80 are shown in the second row of Fig. 11.

VII. DISCUSSION

These inversions provide promising results for using this algorithm within a practical biomedical UT device. The size of the imaging domain is sufficient for biomedical applications such as breast imaging and the contrast values shown are also within the ranges required for such applications. The value of the attenuation in the tissue, which is related to the imaginary part of χ_1^c, was chosen slightly higher than expected values for breast tissue in order to balance out the relative values of the three parameters being inverted. Future work will report on a new balancing technique which we have developed to overcome this constraint, allowing any relative range of values between the reconstructed parameter values. As can be seen from the figures, the quantitative values for the inverse of density, χ_2, are not reconstructed as

well as for the complex contrast of compressibility. This is most certainly due to the fact that the inverse of density shows up in the more complicated field operator, Eq. (25), which includes gradient and divergence operations within the integral. These differential operators were discretized using simple finite differences and thus the numerical approximation may not be sufficient to recover the inverse of density in the inversions. Similar observations were made in Ref. 21.

Although the inversions take several hours of computation time, the algorithm is well suited to parallelization and the time could easily be reduced. Extending the algorithm to full 3D inversions is straight-forward from an algorithmic perspective, but computation time will certainly have to be reduced. Future work will investigate the application of this algorithm to physically realistic breast phantoms, the extension to 3D, and the use of experimental scattered-field data from an in-house UT system.

VIII. CONCLUSION

In this paper, we have presented an inversion algorithm to simultaneously reconstruct three properties of the OI. This algorithm requires a fast and efficient forward solver to compute the scattering from objects with inhomogeneous density, attenuation, and compressibility profiles. The presented forward solver requires the use of the adjoint of the operator which governs the scattering phenomenon in the imaging domain. To make use of this forward solver for large domain problems, three computational features have been implemented. The first provides a good initial guess to make the convergence of the algorithm faster. The second provides an efficient way for storing the elements of the matrix, and the third provides an FFT matrix-vector multiplication for the algorithm. Inversion results for synthetically generated data representative of data that would be collected in a UT system designed for breast imaging are shown. The inversion algorithm produces three images in each of the three properties of the OI. Although the OI is qualitatively reconstructed well in all three images, the quantitative value of the inverse density profile is not as well reconstructed as are the two images associated with the complex contrast of compressibility. A procedure for enhancing the accuracy of all three reconstructions using a novel balancing technique is the topic of future work, which will also investigate the use of the algorithm on more realistic breast phantoms.

[1]P. Mojabi and J. LoVetri, "Simultaneous reconstruction of compressibility and density profiles in multiple frequency acoustic inverse scattering," in *APS/URSI Symposium*, 2013.
[2]M. Haynes and M. Moghaddam, "Large-domain, low-contrast acoustic inverse scattering for ultrasound breast imaging," IEEE Trans. Biomed. Eng. **57**(11), 2712–2722 (2010).

1824   J. Acoust. Soc. Am., Vol. 137, No. 4, April 2015

P. Mojabi and J. LoVetri: Ultrasound tomography

[3] P. Mojabi and J. LoVetri, "A fast and efficient MoM forward solver for ultrasound tomography of inhomogeneous compressibility and density profiles," in *APS/URSI Symposium*, 2013.

[4] P. Mojabi, "Ultrasound tomography: An inverse scattering approach," MSc. dissertation, University of Manitoba, 2014.

[5] M. Moghaddam and W. C. Chew, "Simultaneous inversion of compressibility and density in the acoustic inverse problem," Inverse Probl. **9**(6), 715–730 (1993).

[6] R. J. Lavarello and M. L. Oelze, "Density imaging using inverse scattering," J. Acoust. Soc. Am. **125**(2), 793–802 (2009).

[7] M. Moghaddam, W. C. Chew, and M. Oristaglio, "Comparison of the Born Iterative Method and Tarantolas Method for an electromagnetic time-domain inverse problem," Int. J. Imaging Syst. Technol. **3**(4), 318–333 (1991).

[8] Y. M. Wang and W. C. Chew, "An iterative solution of the two-dimensional electromagnetic inverse scattering problem," Int. J. Imaging Syst. Technol. **1**(1), 100–108 (1989).

[9] P. Mojabi and J. LoVetri, "Comparison of TE and TM inversions in the framework of the Gauss-Newton Method," IEEE Trans. Antennas Propag. **58**(4), 1336–1348 (2010).

[10] W. Chew, G. Otto, W. H. Weedon, J. H. Lin, and Y. M. Wang, "Nonlinear diffraction tomography the use of inverse scattering for imaging," Int. J. Imaging Syst. Technol. **1**, 120–129 (1993).

[11] J. W. Wiskin, D. T. Borup, and S. A. Johnson, "Inverse scattering from arbitrary two-dimensional objects in stratified environments via a Greens operator," J. Acoust. Soc. Am. **102**(2), 853–864 (1997).

[12] O. Haddadin, S. Lucas, and E. Ebbini, "Solution to the inverse scattering problem using a modified distorted Born iterative algorithm," in *IEEE Proceedings of the Ultrasonics Symposium*, Vol. 2, pp. 1411–1414 (1995).

[13] J. Wiskin, D. T. Borup, S. A. Johnson, and M. Berggren, "Non-linear inverse scattering: High resolution quantitative breast tissue tomography," J. Acoust. Soc. Am. **131**(5), 3802–3813 (2012).

[14] A. J. Hesford and W. C. Chew, "Fast inverse scattering solutions using the distorted Born iterative method and the multilevel fast multipole algorithm," J. Acoust. Soc. Am. **128**(2), 679–690 (2010).

[15] F. Lin, A. I. Nachman, and R. C. Waag, "Quantitative imaging using a time-domain eigenfunction method," J. Acoust. Soc. Am. **108**(3), 899–912 (2000).

[16] T. D. Mast, A. I. Nachman, and R. C. Waag, "Focusing and imaging using eigenfunctions of the scattering operator," J. Acoust. Soc. Am. **102**(2), 715–725 (1997).

[17] S. A. Goss, R. L. Johnston, and F. Dunn, "Comprehensive compilation of empirical ultrasonic properties of mammalian tissues," J. Acoust. Soc. Am. **64**(2), 423–457 (1978).

[18] E. L. Madsen, W. A. Berg, E. B. Mendelson, and G. R. Frank, "Anthropomorphic breast phantoms for qualification of investigators for ACRIN protocol 6666," Radiology **239**(3), 869–874 (2006).

[19] R. Lavarello and M. Oelze, "Two approaches for tomographic density imaging using inverse scattering," in *IEEE Ultrasonics Symposium*, 2008, pp. 1298–1301.

[20] A. J. Hesford and R. C. Waag, "Reduced-rank approximations to the far-field transform in the gridded fast multipole method," J. Comput. Phys. **230**(10), 3656–3667 (2011).

[21] S.-J. Kwon and M.-K. Jeong, "Ultrasound inverse scattering determination of speed of sound, density, and absorption," in *IEEE Proceedings of Ultrasonics Symposium*, Vol. 2, 1998, pp. 1631–1634.

[22] R. Harrington, *Time-harmonic Electromagnetic Fields* (McGraw-Hill, New York, 1961).

[23] J. Richmond, "Scattering by a dielectric cylinder of arbitrary cross section shape," IEEE Trans. Antennas Propag. **13**(3), 334–341 (1965).

[24] R. Harrington, *Field Computation by Moment Methods* (Wiley-IEEE Press, Piscataway, NJ, 1993).

[25] L. Jebli, "A comparison of two methods for solving electromagnetic field integral equation," Int. J. Diff. Eq. **2011**, 1–9.

[26] M. R. Hestenes and E. Stiefel, "Methods of conjugate gradients for solving linear systems," J. Res. Natl. Bur. Stand. **49**(6), 409–436 (1952).

[27] B. E. Barrowes, F. L. Teixeira, and J. A. Kong, "Fast algorithm for matrix-vector multiply of asymmetric multilevel block-Toeplitz matrices in 3-D scattering," Microwave Opt. Tech. Lett. **31**(1), 28–32 (2001).

[28] T. Chan and J. Olkin, "Circulant preconditioners for Toeplitz-block matrices," Numer. Algorith. **6**(1), 89–101 (1994).

[29] M. Moghaddam and W. Chew, "Variable density linear acoustic inverse problem," Ultrason. Imag. **15**(3), 255–266 (1993).

[30] A. J. Hesford and R. C. Waag, "The fast multipole method and Fourier convolution for the solution of acoustic scattering on regular volumetric grids," J. Comput. Phys. **229**, 8199–8210 (2010).

[31] W. C. Chew, *Waves and Fields in Inhomogeneous Media (Electromagnetic Waves)* (IEEE Computer Society Press, Piscataway, NJ, 1995).

[32] J. De Zaeytijd, A. Franchois, C. Eyraud, and J. M. Geffrin, "Full wave three-dimensional microwave imaging with a regularized Gauss Newton method theory and experiment," IEEE Trans. Antennas Propag. **55**(11), 3279–3292 (2007).

[33] A. Tijhuis and A. Zwamborn, "Marching on in anything: Solving electromagnetic field equations with a varying physical parameter," Ultra-Wideband, Short-Pulse Electromag. **5**, 655–662 (2002).

[34] A. Tijhuis, K. Belkebir, A. Litman, and B. De Hon, "Theoretical and computational aspects of 2-D inverse profiling," IEEE Trans. Geosci. Remote Sens. **39**(6), 1316–1330 (2001).

[35] R. H. Chan and M. K. Ng, "Conjugate gradient methods for Toeplitz systems," SIAM Rev. **38**(3), 427–482 (1996).

[36] J. W. Cooley and J. W. Tukey, "An algorithm for the machine calculation of complex Fourier series," Math. Comput. **19**(90), 297–301 (1965).

[37] P. C. Hansen, "Deconvolution and regularization with Toeplitz matrices," Numer. Algorith. **29**, 323–378 (2002).

[38] C. Van Loan, *Computational Frameworks for the Fast Fourier Transform* (Society for Industrial and Applied Mathematics, Philadelphia, PA, 1992).

[39] M. Moghaddam and W. C. Chew, "Nonlinear two dimensional velocity profile inversion using time domain data," IEEE Trans. Geosci. Remote Sens. **30**(1), 147–156 (1992).

[40] T. J. Cui, W. C. Chew, X. Yin, and W. Hong, "Study of resolution and super resolution in electromagnetic imaging for half-space problems," IEEE Trans. Antennas Propag. **52**(6), 1398–1411 (2004).

[41] P. Mojabi and J. LoVetri, "Enhancement of the Krylov subspace regularization for microwave biomedical imaging," IEEE Trans. Med. Imag. **28**(12), 2015–2019 (2009).

[42] T. Rubk, P. Meaney, P. Meincke, and K. Paulsen, "Nonlinear microwave imaging for breast-cancer screening using Gauss Newtons method and the CGLS inversion algorithm," IEEE Trans. Antennas Propag. **55**(8), 2320–2331 (2007).

[43] P. C. Hansen, *Rank-deficient and Discrete Ill-posed Problems: Numerical Aspects of Linear Inversion* (Society for Industrial and Applied Mathematics, Philadelphia, PA, 1998).

[44] P. Hansen, "Regularization tools: A MATLAB package for analysis and solution of discrete ill-posed problems," Numer. Algorith. **6**(1), 1–35 (1994).

[45] R. Waag and R. Fedewa, "A ring transducer system for medical ultrasound research," IEEE Trans. Ultrason., Ferroelectr., Freq. Control **53**(10), 1707–1718 (2006).

[46] N. Duric, P. Littrup, S. Schmidt, C. Li, O. Roy, L. Bey-Knight, R. Janer, D. Kunz, X. Chen, J. Goll, A. Wallen, F. Zafar, V. Allada, E. West, I. Jovanovic, K. Li, and W. Greenway, "Breast imaging with the SoftVue imaging system: First results," Proc. SPIE **8675**, 86750K (2013).

[47] R. F. Bloemenkamp, A. Abubakar, and P. M. van den Berg, "Inversion of experimental multi-frequency data using the contrast source inversion method," Inv. Prob. **17**(6), 1611–1622 (2001).

[48] W. Hu, A. Abubakar, and T. Habashy, "Simultaneous multifrequency inversion of full-waveform seismic data," Geophysics **74**(2), R1–R14 (2009).